Materials Advances

ROYAL SOCIETY OF CHEMISTRY

PAPER

View Article Online
View Journal | View Issue

Cite this: *Mater. Adv.*, 2024, 5, 8953

Enhanced piezo-response of mixed-cation copper perovskites with Cl/Br halide engineering†

Amr Elattar, *[abc] Christopher Munoz,[a] Libor Kobera,[d] Andrii Mahun,[d] Jiri Brus,[d] Mohammed Jasim Uddin,[e] Yasuhiko Hayashi,[b] Okenwa Okoli[af] and Tarik Dickens*[a]

Received 25th September 2024,
Accepted 5th October 2024

DOI: 10.1039/d4ma00970c

rsc.li/materials-advances

Halide and cation engineering of organic–inorganic hybrid perovskites has shown a great potential for structural modulation of perovskites and enhancing their optoelectronic properties. Here, we studied the impact of Cl/Br halide engineering on the structural and piezoelectric properties of MA/Cs mixed-cation Cu-perovskite crystals. X-ray diffraction, Raman spectroscopy, and ^{133}Cs solid-state NMR were utilized to find out the nature of the perovskite crystal structure formation. Three distinct crystal structures were obtained depending on the Cl/Br content. High Cl content resulted in the formation of Br-doped (Cs/MA)$CuCl_3$ perovskite with the presence of paramagnetic Cu^{2+} ions. High Br content led to the formation of Cl-doped $(MA/Cs)_2CuBr_4$ perovskite with the presence of diamagnetic Cu^{+} ions. Equimolar Cl/Br perovskite content gave a novel crystal structure with the formation of well-dispersed diamagnetic domains. Compared to the high Cl/Br containing perovskites, the equimolar Cl/Br perovskite revealed the highest potential for piezoelectric applications with a maximum recordable piezoelectric output voltage of 5.0 V. The results provide an insight into the importance of mixed-halide and mixed-cation engineering for tailoring the perovskite structural properties towards a wide range of efficient optoelectronics.

Introduction

Organic–inorganic hybrid perovskite materials have recently made a dramatic and rapid impact on optoelectronic applications owing to their low processing cost, suitable bandgap, high absorption coefficient, and superior carrier transport.[1–6] Halide perovskites have the general formula ABX_3, where A is an organic or inorganic cation, B is metal, and X is halide.[7] Lead and tin-based halide perovskites have acquired the most perovskite-related research interest. However, the environmental concerns of toxic lead (Pb) and easily oxidized tin (Sn) hinder their commercialization.[8,9] Alternatively, highly stable copper-based halide perovskites are deemed one of the next generation of lead-free perovskites to be emerging in photovoltaics,[10] energy storage,[11] piezoelectric,[12] lighting emitting diodes,[13] thermoelectric,[14] and thermochromic smart windows applications.[15]

Structural modulation of halide perovskites, in terms of A-site, B-site, and X-site engineering, has revealed its potential to explore new perovskites with unique properties. One of the most common A-site engineering routes is inorganic cesium (Cs)/organic methyl ammonium (MA) mixed-cations alloying. Premkumar *et al.* reported highly ordered $MA_{1-x}Cs_xPbBr_3$ mixed phase structures with suppressing of non-radiative recombination through incorporation of Cs^{+} cations in the $MAPbBr_3$ crystal structure.[16] Further work showed the bimodal bandgap behavior of $MA_{1-x}Cs_xPbBr_3$ single crystals where the bandgaps of mixed-cation perovskites are like those of pure $CsPbBr_3$ for $x > 0.13$ and pure $MAPbBr_3$ for $x \leq 0.13$.[17] Si *et al.* revealed an enhancement of the green emission properties of $MAPbBr_3$ thin film upon Cs-alloying to achieve a maximum external quantum efficiency of ~2.0% for an $MA_{0.6}Cs_{0.4}PbBr_3$ perovskite thin film-based device.[18] Cs-doping (2%) was found to enhance the photodetection property of $MAPbBr_3$ single crystal owing to the reduction in trap density of the mixed-cation perovskite single crystal.[19] Other work discussed

[a] *Industrial & Manufacturing Engineering, FAMU-FSU College of Engineering, 2525 Pottsdamer St., Tallahassee, Florida, 32310, USA. E-mail: ae23e@fsu.edu, dickens@eng.famu.fsu.edu*
[b] *Graduate School of Environmental, Life, Natural Science and Technology, Okayama University, 3-1-1 Tsushimanaka, Kita-ku, Okayama, 700-8530, Japan*
[c] *Department of Chemistry, Faculty of Science, Ain Shams University, Cairo, 11566, Egypt*
[d] *Institute of Macromolecular Chemistry of the Czech Academy of Sciences, Heyrovskeho nam. 2, 162 06, Prague 6, Czech Republic*
[e] *Photonics and Energy Research Laboratory (PERL), Department of Mechanical Engineering, The University of Texas, Rio Grande Valley, 1201 West University Drive, Edinburg, Texas 78539, USA*
[f] *Herff College of Engineering, University of Memphis, Memphis, TN, 38111, USA*
† Electronic supplementary information (ESI) available. See DOI: https://doi.org/10.1039/d4ma00970c

different morphologies such as porous sheets, nanorods and nanowires, fiber structures, and tightly bonded grains upon mixing $MAPbI_3$ with various amounts of Cs ions.[20]

Most of the previous literature focused on the impact of Cs/MA mixed-cations engineering of lead-based perovskite materials. However, a few research works were reported concerning Cs/MA mixed-cations engineering of lead-free perovskite materials.[21] Regarding our previous work, a two-dimensional phase-pure MA/Cs mixed-cation Cu-based perovskite crystal can be obtained by using an equal concentration of A-site cations $[MA^+] = [Cs^+]$ and X-site halides $[Cl^-] = [Br^-]$ as well through the perovskite precursor. The as-prepared perovskite exhibits a reduced bandgap (1.53 eV) with enhanced photovoltaic properties compared to single cation-based perovskites.[22] Here, we study the impact of Cl/Br mixed-halides engineering on the structural properties of mixed-cation Cu-perovskite with an equal concentration of A-site cations $[MA^+] = [Cs^+]$.

Piezoelectric materials, showing electrical change under the effect of mechanical strain, have exhibited potential application in power storage, smart sensors, energy harvesters, and artificial actuators.[23] Regarding the literature, $MAPbI_3$ and $FAPbBr_3$ lead-based halide perovskite materials have emerged in piezoelectric generators owing to their light-induced piezoelectric properties.[24–26] You *et al.* reported a non-centrosymmetric TMCM–$MnCl_3$ perovskite structure with significant enhancement of piezoelectric properties, where TMCM = trimethylchloromethylammonium cation.[27] Generally, embedding of piezoelectric perovskite particles through polymeric materials was found to enhance the overall piezoelectric performance.[28] For instance, Huang *et al.* reported a great enhancement of piezoelectric properties of MA_2CuCl_4/PVDF composite film with a 7 times higher piezoelectric response than PVDF film.[12] In this work, we study the piezoelectric potential of (Cs/MA) mixed-cation (Cl/Br) mixed-halide copper perovskites with embedding through the most common polymer utilized for piezoelectric devices: polydimethylsiloxane (PDMS) polymer matrix.

Experimental

Materials

Cesium bromide CsBr (≥99%), cesium chloride CsCl (≥99%), copper bromide $CuBr_2$ (≥99%), copper chloride $CuCl_2$ (≥99%), methylammonium chloride MACl (≥99%), and methylammonium bromide MABr (≥99%), as raw materials were purchased from Sigma-Aldrich. Deionized water was used as the solvent for the perovskite crystal growth. All reagents and solvents were used without further purification.

Synthesis of $(CH_3NH_3)_2CuCl_{4-x}Br_x$ single crystals

As depicted in Table 1, saturated aqueous solutions of different molar ratios of cesium halide CsX (1.5 mmol), methylammonium halide MAX (1.5 mmol), and cupric halide CuX_2 (2 mmol) were prepared *via* dissolving the perovskite precursors in 2 mL deionized water using VORTEX for 5 min. The dissolved solutions were filtered *via* a 0.45 μm PVDF syringe filter. Then, the resultant solutions were left for two weeks, at room temperature, to get single crystals of (Cs/MA) mixed-cations (Cl/Br) mixed-halides copper perovskites.

Table 1 Molar ratios of raw solute materials used for preparing mixed-halide Cu-perovskites

CsCl (mol)	CsBr (mol)	MACl (mol)	MABr (mol)	$CuCl_2$ (mol)	$CuBr_2$ (mol)	Perovskite abbreviation
1.5	w/o	1.5	w/o	2.0	w/o	Cl_7
1.5	w/o	w/o	1.5	2.0	w/o	$Cl_{5.5}Br_{1.5}$
w/o	1.5	w/o	1.5	2.0	w/o	Cl_4Br_3
1.5	w/o	1.5	w/o	w/o	2.0	Cl_3Br_4
w/o	1.5	1.5	w/o	w/o	2.0	$Cl_{1.5}Br_{5.5}$
w/o	1.5	w/o	1.5	w/o	2.0	Br_7

Fabrication of perovskite/PDMS piezoelectric sensors

The sensor was fabricated using SYLGRAD 184 silicone elastomer kit as the source of PDMS and the curing agent. 10 wt% of perovskite powder samples were mixed with 10 : 1 (V/V) of "PDMS base material : curing agent" mixture, and stirred slowly for 20 min. This mixture was then poured into a 1 × 1 $inch^2$ glass mold and heated to 100 °C for 30 min to accelerate the curing time. After fully curing, copper tape, used as electrodes, was added to both sides of the film. Finally, the copper-taped film was surrounded with Kapton tape to shield from any external electrical effect.

Characterization

The perovskite morphological structure was confirmed *via* scanning electron microscopy (SEM) (JEOL) with energy dispersive spectroscopy (EDS) to obtain an elemental mapping to measure the Cl/Br content. Raman vibrational modes (JASCO, NRS4500 NMDS) were obtained using 532 nm excitation (green) lasers to characterize perovskite crystal lattice vibrations. X-ray diffraction (XRD) measurements were performed using a Rigaku Smart lab diffractometer at a wavelength of 1.5406 Å. Rietveld refinement was performed by GSASII program. Thermogravimetric analysis was conducted by TGA (TA Instruments). A Keysight Infinnivision DSOX3024T digital storage oscilloscope was used for measuring piezoelectric properties.

Solid-state nuclear magnetic resonance analysis

The ^{133}Cs and ^{1}H solid-state NMR spectra (ssNMR) were recorded at 11.7 T using a Bruker AVANCE III HD spectrometer and a 2.5 mm cross-polarization magic angle spinning (CP/MAS) probe operating at the Larmor frequency of $\nu(^{133}Cs)$ = 65.611 MHz and $\nu(^{1}H)$ = 500.180 MHz, respectively, and the following techniques were applied: (i) ^{1}H and ^{133}Cs VF/MAS NMR experiments; (ii) the ^{133}Cs spin–lattice relaxation times $T_1(^{133}Cs)$ were measured using the saturation recovery and inversion recovery experiments. A temperature of 298 K was maintained for all NMR experiments and the temperature calibration was performed on $Pb(NO_3)_2$.[29] Dried samples were packed into ZrO_2 rotors and stored at laboratory temperature. All NMR spectra and relaxation build-up dependencies were

processed using the Top Spin 3.5 pl2 software package. Detailed experimental parameters are provided in the ESI.†

Results and discussion

Six different mixed halides (Cl/Br) of 50% mixed-cations (Cs/MA)-based copper perovskite crystals were synthesized *via* slow evaporation of aqueous saturated solutions containing 1.5 : 1.5 : 2 molar ratios of CsX : MAX : CuX_2, respectively, where X = Cl or Br. Photographs of mixed halides/cations Cu perovskite crystals with different Cl/Br precursor ratios are shown in Fig. 1a. Upon increasing Br-content in the precursor solution, three major perovskite sets, whose colors are reddish-orange, brown, and brownish black, were obtained for Cl_7–$Cl_{5.5}Br_{1.5}$, Cl_4Br_3–Cl_3Br_4, and $Cl_{1.5}Br_{5.5}$–Br_7 mixed cation/halide perovskite crystal sets, respectively. This color transition was further confirmed after grinding the crystals, as depicted in Fig. 1b. Different morphological structures were observed microscopically for perovskite crystals by scanning electron microscope (SEM), as shown in Fig. S1a (ESI†). Gradual increases and decreases of Br% and Cl%, respectively, through perovskite samples were confirmed by energy dispersive spectroscopy (EDS), as presented in Fig. 1c. The atomic compositions of Cl (%) and Br (%) vary among the three previously designated main categories. The Br compositions of the perovskite sets (Cl_7–$Cl_{5.5}Br_{1.5}$, Cl_4Br_3–Cl_3Br_4, and $Cl_{1.5}Br_{5.5}$–Br_7) are in the range (0–5%, 20%, and 35–45%), respectively. EDS elemental mapping is presented in Fig. S1b and c (ESI†).

Powder X-ray diffraction (XRD) measurements performed for the perovskite powder samples reveal the appearance of three distinct crystal structures (as shown in Fig. 2a) that relate to the three distinct EDS sets. Both the (Cl_7–$Cl_{5.5}Br_{1.5}$) and the ($Cl_{1.5}Br_{5.5}$–Br_7) sets exhibit the same crystal structure as $CsCuCl_3$ and Cs_2CuBr_4, respectively. Meanwhile, the third (Cl_4Br_3–Cl_3Br_4) perovskite set exhibits a novel mixed cations/halides crystal structure. According to literature,[30,31] Cl_7 and Br_7 perovskites have a distorted hexagonal *P*6122 crystal structure and an orthorhombic *Pnma*(62) crystal structure, respectively (as depicted in Fig. S2 and S3, ESI†). Generally, the diffraction patterns of each perovskite set shift obviously toward smaller 2θ angles upon Br addition due to the larger effective ionic radius of Br^- (196 pm) compared to Cl^- (181 pm). As a result, $Cl_{5.5}Br_{1.5}$ and $Cl_{1.5}Br_{5.5}$ perovskites are supposed to be MA/Br-doped $CsCuCl_3$ and MA/Cl-doped Cs_2CuBr_4 perovskites, respectively. Rietveld refinement was performed to confirm this behavior, as depicted in Fig. S4 (ESI†), which is consistent with previous literature.

Raman vibrational modes of the mixed cations/halides perovskites were examined in the range (50–500 cm^{-1}) to further prove their trimodal behavior, as depicted in Fig. 2b. Three different Raman modes were obtained from the three perovskite sets which are consistent with their three different crystal structures, as ascribed in XRD measurements. In the (Cl_7–$Cl_{5.5}Br_{1.5}$) perovskite category, three Raman modes, around 115, 180, and 285 cm^{-1}, are assigned to $\omega(E_2)$, the X–Cu–X wagging, $\tau(E_2)$, the X–Cu–X twisting/torsion, and $\nu_s(E_2)$, the X–Cu–X symmetric stretching, where X is Cl and/or Br, respectively. Meanwhile, the ($Cl_{1.5}Br_{5.5}$–Br_7) perovskite category Raman mode around 184 cm^{-1} is ascribed to the symmetric Cu–Br stretching mode. It is worth noting that the (Cl_4Br_3–Cl_3Br_4) perovskite set has a similar Raman modes behaviour as the (Cl_7–$Cl_{5.5}Br_{1.5}$) perovskite set with blue shifting of the second Raman peak toward higher wavenumber around 200 cm^{-1}.

^{133}Cs solid-state NMR (ssNMR) analyses were performed on the copper-based perovskites with mixed halides (Cl/Br) and mixed counterions (MA/Cs). To gain deeper insight into the structure of the prepared systems, ^{133}Cs VF/MAS NMR spin-echo[32] and T_1-relaxation experiments[33,34] were conducted. This approach is based on the fact that the presence of unpaired electron(s) induces detectable changes in the chemical shift of observed nuclei and a reduction in ^{133}Cs NMR T_1-relaxation times. The reason for this observation is the fact that the presence of paramagnetic metal centers (*e.g.* Cu^{2+}) causes extremely rapid longitudinal and transverse relaxation of the nearby nuclei due to strong electron–spin couplings.[35,36] The relaxation build-up curves of the detected ^{133}Cs NMR signal(s) were analysed by single-exponential functions and values of $T_1(^{133}Cs)$ relaxation times of individual components are

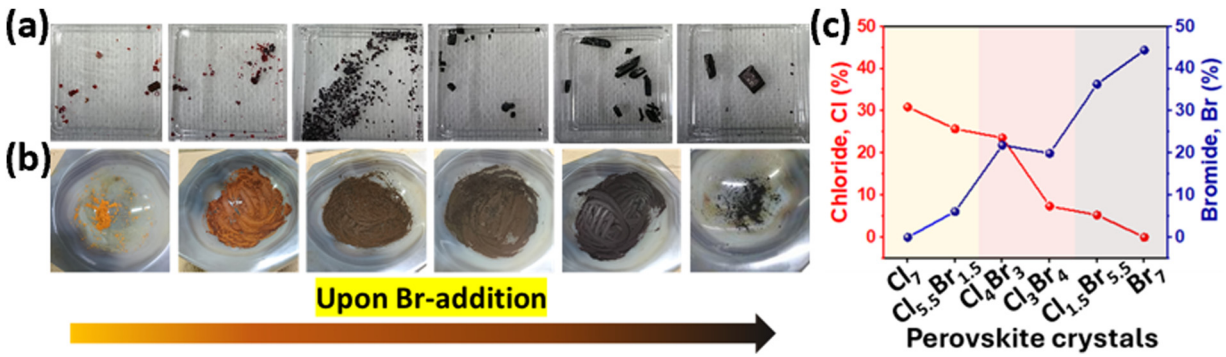

Fig. 1 Copper perovskite crystals prepared *via* the slow evaporation method (a) and after grinding with mortar and pestle (b) where the samples from left to right are: Cl_7, $Cl_{5.5}Br_{1.5}$, Cl_4Br_3, Cl_3Br_4, $Cl_{1.5}Br_{5.5}$, and Br_7, respectively. (c) Data from energy dispersive spectroscopy (EDS) for determining the (Cl/Br) content of perovskite crystals.

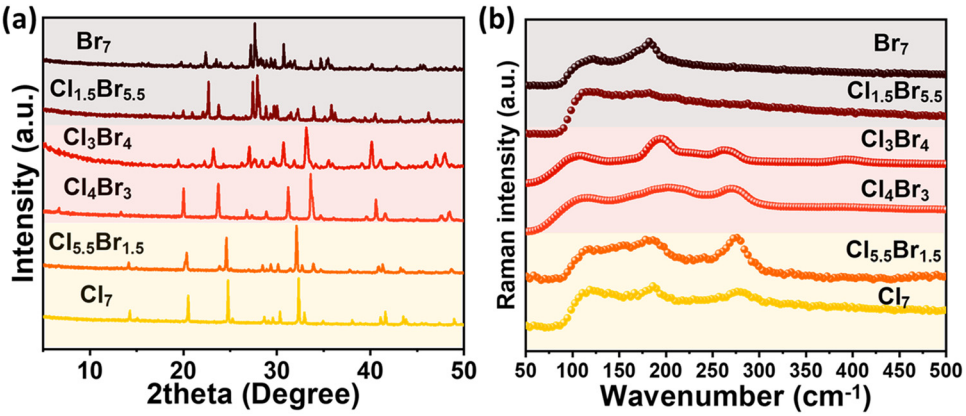

Fig. 2 Powder XRD measurements (a) and Raman measurements (b) of different Cu-perovskite powders.

summarized in Table 2. The inversion-recovery technique was used for spins with fast relaxation behavior, while the saturation-recovery experiment was used for spins with relatively slow relaxation times. The investigated samples can be divided into three groups based on the recorded ^{133}Cs VF/MAS NMR spectra, as depicted in Fig. 3 and Fig. S5 (ESI†).

The first group consists of samples with low bromine content (Cl_7–$Cl_{5.5}Br_{1.5}$), where the dominant NMR signal is located at approximately 1200 ppm (Fig. 3a). The Cl_7 perovskite sample exhibited one symmetric and very narrow signal corresponding to a single crystallographic position of Cs ions. Based on literature data, this signal was attributed to $(Cs/MA)CuCl_3$ which is consistent with XRD and Raman results.[37]

In the case of $Cl_{5.5}Br_{1.5}$ perovskite, which has a slightly increased bromine anion content, two broad, not fully resolved signals at around 1200 ppm and 950 ppm were detected in the ^{133}Cs VF/MAS NMR spectrum. The presence of two signals indicates two preferred positions of Cs^+ ions in the perovskite matrix, where one or more Cl^- anions are replaced by Br atoms, respectively. The incorporation of Br^- into the matrix is random, which is evident from the visible signal broadening in the spectrum of $Cl_{5.5}Br_{1.5}$. However, the similar chemical shift of the detected signals in both systems suggests a similar crystallographic group, as discussed in the XRD section, with slight distortion in the symmetry group for $Cl_{5.5}Br_{1.5}$ perovskite.

Table 2 The ^{133}Cs spin–lattice relaxation times $T_1(^{133}Cs)$ with relative amount determined for each spectral component of the perovskite samples

^{133}Cs spin–lattice relaxation times $T_1(^{133}Cs)$ [s, ms]					
Sample/δ_{iso}	1200 ppm	950 ppm	294 ppm	215 ppm	165 ppm
Cl_7	13.5 ms	—	—	—	—
$Cl_{5.5}Br_{1.5}$	15 ms	24.5 ms	—	—	—
Cl_4Br_3	—	—	25 ms	750 ms	10 s
Cl_3Br_4	—	—	—	750 ms	14 s
Sample/δ_{iso}	2900 ppm	2750 ppm	600 ppm	155 ppm	145 ppm
$Cl_{1.5}Br_{5.5}$	2 ms	13.3 ms	6 ms	—	—
Br_7	2 ms	—	6 ms	15 s	31 s

Moreover, the detected signals in both systems show a significant upfield shift of the ^{133}Cs NMR signals, indicating the close proximity of unpaired electrons (Cu^{2+}) to Cs counterions. Clear evidence of the presence of paramagnetic Cu^{2+} ions is provided by the ^{133}Cs spin–lattice relaxation experiments, which yield very fast $T_1(^{133}Cs)$ times of around 20 ms, as shown in Table 2. The ^{133}Cs spin–lattice relaxation processes were monitored using the inversion-recovery technique and easily described using a single-exponential function for all three signals, which indicates uniform distribution/dispersion of the ions within the domains.

The second (Cl_4Br_3–Cl_3Br_4) perovskite group can be defined as the systems with equimolar chlorine and bromine contents. In these samples, the dominant NMR signal was detected at 215 ppm, as depicted in Fig. 3b, indicating copper-based perovskites with an equal ratio of chlorine and bromine. In the case of the Cl_4Br_3 sample, two additional signals were detected with chemical shifts of 294 ppm and 165 ppm, respectively. The signal at 294 ppm was attributed to chlorine-rich domains with $T_1(^{133}Cs)$ time 25 ms, while the signal at 165 ppm was attributed to bromine-rich domains. Furthermore, the observed $T_1(^{133}Cs)$ time of the bromine-rich domains is around 10 s. The Cl_3Br_4 sample, with a higher bromine content, exhibited only two relatively sharp signals at 215 ppm and 161 ppm, corresponding to the copper-based perovskite with an equal ratio of halides phase and bromine-rich domains, respectively. Additionally, this sample was probed by a ^{133}Cs VF/MAS NMR experiment with a long repetition delay of 100 s, as shown in the inset of Fig. 3b, where the signal intensity of the bromine-rich domains is significantly increased. Similar behavior also confirms the ^{133}Cs spin–lattice relaxation experiments with similar $T_1(^{133}Cs)$ times, as shown in Table 2. These results suggest that the bromine-rich domains form a homogeneously dispersed phase where Cu^{2+} is reduced to Cu^{1+} (in other words, no effect of paramagnetic centers was observed in this phase) with domain size >20 Å. The spin–lattice ^{133}Cs relaxation process was monitored using the saturation-recovery technique for the spins resonating at 165 ppm, while an inversion-recovery experiment was applied for the spins resonating at 215 ppm and 294 ppm (Table 2).

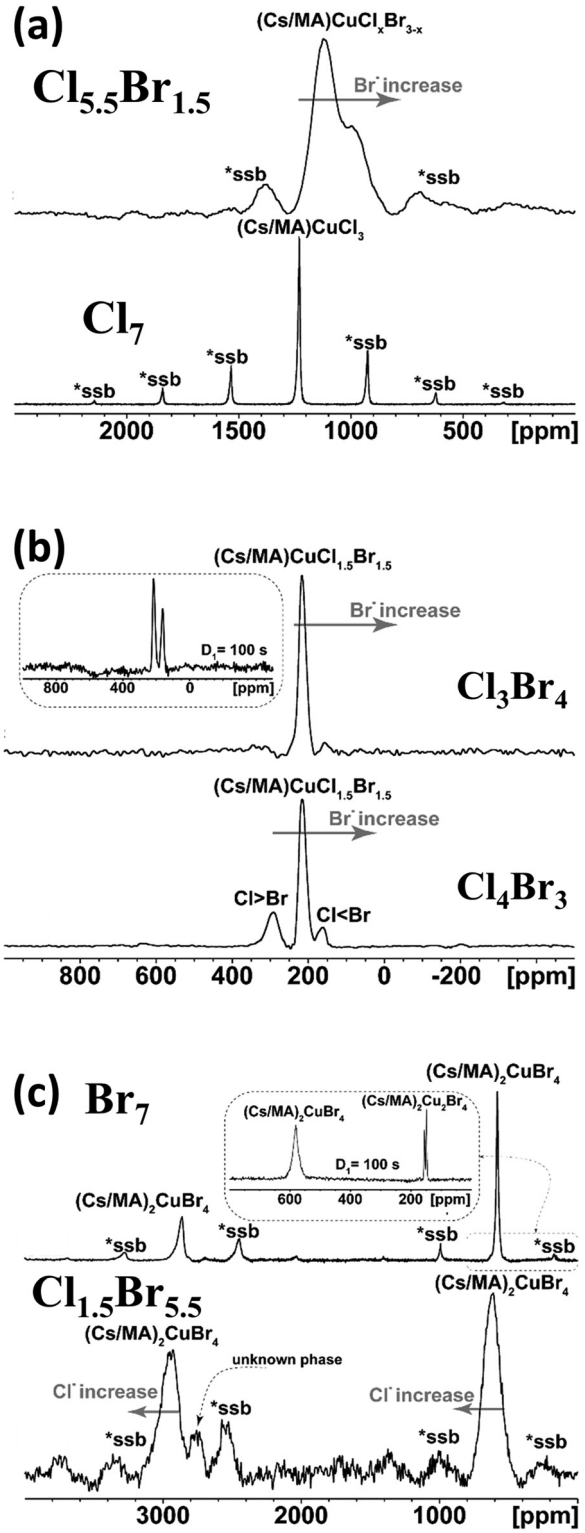

Fig. 3 Experimental ^{133}Cs VF/MAS NMR spectra of (a) Cl_7, $Cl_{5.5}Br_{1.5}$, (b) Cl_4Br_3, Cl_3Br_4, and (c) $Cl_{1.5}Br_{5.5}$, Br_7, respectively. The asterisks (*ssb) denote spinning sidebands.

The last group can be defined as high bromine content ($Cl_{1.5}Br_{5.5}$–Br_7), and corresponding ^{133}Cs VF/MAS NMR spectra are depicted in Fig. 3c. The ^{133}Cs VF/MAS NMR spectrum of the Br_7 sample (fully bromine perovskite) exhibited two sharp and symmetric signals at *ca.* 2900 ppm and 600 ppm, respectively. Based on literature data, these two signals correspond to two different Cs sites in $(MA/Cs)_2CuBr_4$, which is consistent with XRD and Raman data.[38] The determined $T_1(^{133}Cs)$ times of 2 ms and 6 ms, respectively, clearly confirm the presence of paramagnetic Cu^{2+} ions in close proximity. Furthermore, two additional diamagnetic Cs sites at 145 and 155 ppm were observed in the case of the ^{133}Cs VF/MAS NMR experiment with a 100 s recycle delay (Fig. 3c, inset). The diamagnetic nature of these detected signals was confirmed using the $T_1(^{133}Cs)$ relaxation experiment, where $T_1(^{133}Cs)$ times of 31 s and 15 s, respectively, were determined. This also indicates that the $(MA/Cs)_2CuBr_4$ system forms well-dispersed diamagnetic domains within the investigated matrix.

For the $Cl_{1.5}Br_{5.5}$ sample, two broad dominant signals with similar chemical shifts and $T_1(^{133}Cs)$ times as for Br_7 sample were detected. The broadening reflects the random distribution of Cl^-/Br^- anions in the perovskite matrix and suggests the formation of a fully amorphous system. Moreover, a broad extra signal appeared at around 2750 ppm, which was assigned to a minor unknown but paramagnetic phase (see Table 2). In this case, the relaxation process is very fast, and the corresponding build-up curve is noisy. Consequently, the determined relaxation time, $T_1(^{133}Cs)$ = 13.30 ms, should be considered relatively uncertain.

Moreover, the wide dispersion of the ^{133}Cs NMR shifts and the fast $T_1(^{133}Cs)$ times of all detected signals (2900 ppm, 2750 ppm, 600 ppm) suggest the presence of diamagnetic and paramagnetic domains with random distribution in the perovskite matrix. Generally, it can be concluded that the increase in Br^- anions induces the formation of well-dispersed diamagnetic domains, where copper is reduced from Cu^{2+} to Cu^{1+} with roughly estimated domain sizes up to 40 Å.

The presence of the second, organic counterion, methylammonium (MA), in all investigated systems, was confirmed by ^{1}H VF/MAS NMR experiments, as shown in Fig. 4. Furthermore, ^{1}H VF/MAS NMR provides not only information about the presence of the organic counterion but also suggests ordering of MA molecules in Cu-based perovskites. The ^{1}H VF/MAS NMR spectra clearly indicate that MA counterions in fully chlorine-containing Cl_7 and fully bromine-containing Br_7 perovskites are well ordered. Additionally, a trend is observed where an increased concentration of Br^- anions in the matrix leads to a more disordered arrangement of MA counterions. This trend is exemplified by the $Cl_{1.5}Br_{5.5}$ sample, where only a broad and unresolved signal was detected. This observation is consistent with the ^{133}Cs VF/MAS NMR spectrum of the $Cl_{1.5}Br_{5.5}$ sample (Fig. 3c), which also suggests the presence of disordered Cs^+ counterions.

The thermal stability of the mixed cations Cu-perovskites was studied through thermogravimetric analysis (TGA). The decomposition profiles for Cl_7, Cl_4Br_3, and Br_7 Cu perovskites are composed of two steps, as shown in Fig. S6 (ESI†). The first step is accompanied by weight loss of both organic ammonium halides (MAX) and cesium halides (CsX). The second step is

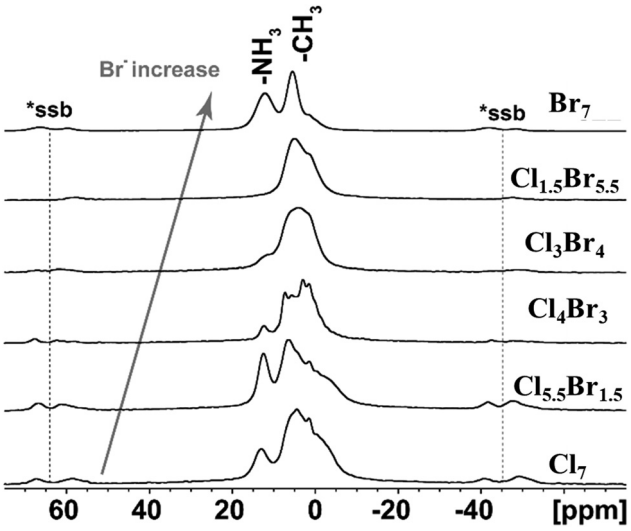

Fig. 4 Experimental ^{1}H VF/MAS NMR (2-loops) spectra of the perovskite samples. The asterisks (*ssb) denote spinning sidebands.

possibly accompanied by the loss of copper halides (CuX_2). The first weight loss is at 320 °C, 190 °C, and 220 °C for Cl_7, Cl_4Br_3, and Br_7 perovskites, respectively, which reveals an increase in the perovskite thermal stability in the order $Cl_4Br_3 < Br_7 < Cl_7$. Different thermal decomposition profiles of perovskite samples corroborate their different crystal structures which are consistent with the XRD, Raman, and NMR results.

To explore the piezoelectric potential application of the mixed cations/halides copper-based perovskite samples, we fabricated a "Cu/perovskite–PDMS composite/Cu" cell configuration, as shown in Fig. S7 (ESI†), to measure the piezoelectric response. Fig. 5 exhibits the piezoelectric sensing mechanism under a pressing/releasing process. Upon pressing, voltage is generated owing to the polarization of perovskite particles embedded in the PDMS matrix whereas the releasing process leads to demolishing both the perovskite polarization and the pressure-dependent voltage as well. Regarding the literature,[39] the 10 wt% of PDMS composite materials was supposed to be the optimized concentration for getting the highest piezoelectric response. As a result, all perovskite/PDMS composites were prepared with a 10 wt% perovskite concentration. Fig. 6 exhibits

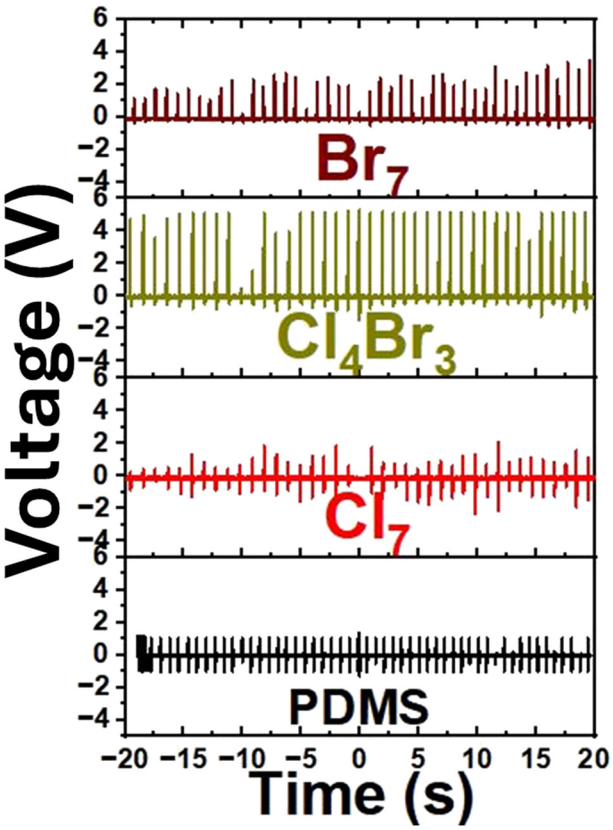

Fig. 6 Piezoelectric properties of the perovskite/PDMS composite films: output voltage of PDMS (black), Cl_7/PDMS (red), Cl_4Br_3/PDMS (yellow), and Br_7/PDMS (dark red) composite films under a periodic pressuring and releasing process with a knocking pen.

the piezo voltage of perovskite/PDMS composites under the periodic pressure/release process with a knocking pen. Under vertical compression, the Cl_7, Cl_4Br_3, and Br_7 perovskite–PDMS composite sensors show 2 times, 5 times, and 3 times higher piezoelectric response than that of the pure PDMS sensor, respectively. Notably, combining of mixed cations/halides copper perovskites with PDMS polymer creates a synergistic effect, leading to enhanced piezoelectric properties owing to their strong interaction between copper perovskites and PDMS polymer. Furthermore, the equimolar Cl/Br content perovskite

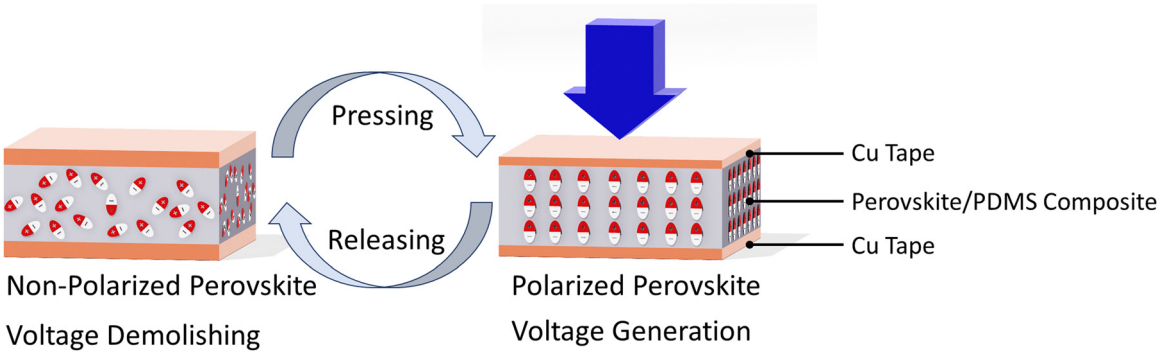

Fig. 5 Piezoelectric sensor configuration and its working mechanism under pressing/releasing process.

matrix, Cl_4Br_3–PDMS composite sensor, shows the highest piezoelectric response rather than that of both high Cl content and high Br content samples, Cl_7–PDMS and Br_7–PDMS composite sensors, respectively. This might be attributed to both the two-dimensional crystallinity and the diamagnetic domains of Cl_4Br_3 perovskite, as discussed in XRD and NMR results. Comparison of output voltage of halide perovskites-based piezoelectric nanogenerators are shown in Table S1 (ESI†). These results reveal the potential of cation/halide engineering of halide perovskites towards fabrication of efficient piezoelectric generators.

Conclusions

In summary, we studied the (Cl/Br) mixed halides engineering of (50%Cs/50%MA) mixed cations copper perovskite. Three distinct crystal structures were obtained depending on the Cl/Br content. The piezoelectric sensors based on the equimolar Cl/Br-mixed cation perovskite showed the highest potential for piezoelectric generation. The key figures of merit revealed in this work highlights the potential of emerging lead-free copper halide perovskites for future commercialization of piezoelectric devices.

Author contributions

Amr Elattar conceived the idea for the manuscript and designed the experiments. Amr Elattar synthesized the materials and conducted SEM, Raman, and XRD characterizations. Libor Kobera and Andrii Mahun conducted and wrote the solid-state NMR analysis. Christopher Munoz conducted the piezoelectric application. Amr Elattar wrote the first manuscript. All authors discussed the results and commented on the manuscript at all stages. Jiri Brus led the assessment of the NMR part. Mohammed Jasim Uddin led the assessment of the piezoelectric application part. Yasuhiko Hayashi, Okenwa Okoli, and Tarik Dickens coordinated the entire project.

Data availability

The data supporting this article has been included as part of the ESI.†

Conflicts of interest

There are no conflicts to declare.

Acknowledgements

Amr Elattar, Tarik Dickens, and Okenwa Okoli acknowledge the NNSA MSIPP I-AM EMPOWER'D (Grant No. DE-NA0004004) at the FAMU-FSU College of Engineering. Libor Kobera, Andrii Mahun and Jiri Brus acknowledge the financial support from the Grant Agency of the Czech Republic (Grant GA24-10199S), Dr Siegrist's lab for XRD usage, and the DOW SURE program for donation of desktop SEM program.

References

1 E. H. Jung, N. J. Jeon, E. Y. Park, C. S. Moon, T. J. Shin, T.-Y. Yang, J. H. Noh and J. Seo, *Nature*, 2019, **567**, 511–515.
2 Z. Liu, J. Hu, H. Jiao, L. Li, G. Zheng, Y. Chen, Y. Huang, Q. Zhang, C. Shen, Q. Chen and H. Zhou, *Adv. Mater.*, 2017, **29**, 1606774.
3 R. Yang, R. Li, Y. Cao, Y. Wei, Y. Miao, W. L. Tan, X. Jiao, H. Chen, L. Zhang, Q. Chen, H. Zhang, W. Zou, Y. Wang, M. Yang, C. Yi, N. Wang, F. Gao, C. R. McNeill, T. Qin, J. Wang and W. Huang, *Adv. Mater.*, 2018, **30**, 1804771.
4 Q. Chen, J. Wu, X. Ou, B. Huang, J. Almutlaq, A. A. Zhumekenov, X. Guan, S. Han, L. Liang, Z. Yi, J. Li, X. Xie, Y. Wang, Y. Li, D. Fan, D. B. L. Teh, A. H. All, O. F. Mohammed, O. M. Bakr, T. Wu, M. Bettinelli, H. Yang, W. Huang and X. Liu, *Nature*, 2018, **561**, 88–93.
5 H. Cho, S.-H. Jeong, M.-H. Park, Y.-H. Kim, C. Wolf, C.-L. Lee, J. H. Heo, A. Sadhanala, N. Myoung, S. Yoo, S. H. Im, R. H. Friend and T.-W. Lee, *Science*, 2015, **350**, 1222–1225.
6 J. Zhao, L. Zhao, Y. Deng, X. Xiao, Z. Ni, S. Xu and J. Huang, *Nat. Photonics*, 2020, **14**, 612–617.
7 A. Kojima, K. Teshima, Y. Shirai and T. Miyasaka, *J. Am. Chem. Soc.*, 2009, **131**, 6050–6051.
8 J. Li, H.-L. Cao, W.-B. Jiao, Q. Wang, M. Wei, I. Cantone, J. Lü and A. Abate, *Nat. Commun.*, 2020, **11**, 310.
9 L. Chen, S. Fu, Y. Li, N. Sun, Y. Yan and Z. Song, *Adv. Sci.*, 2024, **11**, 2304811.
10 I. Hamdi, Y. Khan, F. Aouaini, J. H. Seo, H.-J. Koo, M. M. Turnbull, B. Walker and H. Naïli, *J. Mater. Chem. C*, 2022, **10**, 3738–3745.
11 P. Pandey, N. Sharma, R. A. Panchal, S. W. Gosavi and S. Ogale, *ChemSusChem*, 2019, **12**, 3742–3746.
12 S. Huang, G. Tang, H. Huang, X. Wu, P. Zhou, L. Zou, L. Xie, J. Deng, X. Wang, H. Zhong and J. Hong, *Sci. Bull.*, 2018, **63**, 1254–1259.
13 S. Lin, Z. Ma, X. Ji, Q. Zhou, W. Chu, J. Zhang, Y. Liu, Y. Han, L. Lian, M. Jia, X. Chen, D. Wu, X. Li, Y. Zhang, C. Shan and Z. Shi, *Adv. Mater.*, 2024, **36**, 2313570.
14 Z. Kang, H. Xiong, B. Wu, L. Jiang, B. Fan, A. Yang, B. Sa, J. Li, L. Lin and Y. Qiu, *EcoMat*, 2022, **4**, e12163.
15 A. Elattar, H. Suzuki, R. Mishima, K. Nakao, H. Ota, T. Nishikawa, H. Inoue, A. K. K. Kyaw and Y. Hayashi, *J. Mater. Chem. C*, 2021, **9**, 3264–3270.
16 S. Premkumar, K. Kundu and S. Umapathy, *Nanoscale*, 2019, **11**, 10292–10305.
17 F. Liu, F. Wang, K. R. Hansen and X.-Y. Zhu, *J. Phys. Chem. C*, 2019, **123**, 14865–14870.
18 J. Si, Y. Liu, N. Wang, M. Xu, J. Li, H. He, J. Wang and Y. Jin, *Nano Res.*, 2017, **10**, 1329–1335.
19 L. Li, M. Su, X. Qiu, X. Zhao, X. Zhu, W. Wei, L. Huang, G. Li, Y. Wang and W. H. Sun, *Ceram. Int.*, 2022, **48**, 436–445.
20 G. Murugadoss, R. Thangamuthu, S. Vijayaraghavan, H. Kanda and S. Ito, *Electrochim. Acta*, 2017, **257**, 267–280.
21 M. S. Adli Azizman, A. W. Azhari, N. Ibrahim, D. S. Che Halin, S. Sepeai, N. A. Ludin, M. N. Md Nor and L. N. Ho, *Heliyon*, 2024, **10**, e29676.

22 A. Elattar, W. Li, H. Suzuki, T. Kambe, T. Nishikawa, A. K. K. Kyaw and Y. Hayashi, *Chem. – Eur. J.*, 2022, **28**, e202104316.
23 C. R. Bowen, H. A. Kim, P. M. Weaver and S. Dunn, *Energy Environ. Sci.*, 2014, **7**, 25–44.
24 M. Coll, A. Gomez, E. Mas-Marza, O. Almora, G. Garcia-Belmonte, M. Campoy-Quiles and J. Bisquert, *J. Phys. Chem. Lett.*, 2015, **6**, 1408–1413.
25 T. Paul, S. Maiti, U. Mukherjee, S. Mondal, A. Sahoo and K. K. Chattopadhyay, *Mater. Lett.*, 2021, **301**130264.
26 Y.-J. Kim, T.-V. Dang, H.-J. Choi, B.-J. Park, J.-H. Eom, H.-A. Song, D. Seol, Y. Kim, S.-H. Shin, J. Nah and S.-G. Yoon, *J. Mater. Chem. A*, 2016, **4**, 756–763.
27 Y.-M. You, W.-Q. Liao, D. Zhao, H.-Y. Ye, Y. Zhang, Q. Zhou, X. Niu, J. Wang, P.-F. Li, D.-W. Fu, Z. Wang, S. Gao, K. Yang, J.-M. Liu, J. Li, Y. Yan and R.-G. Xiong, *Science*, 2017, **357**, 306–309.
28 H. Park, C. Ha and J.-H. Lee, *J. Mater. Chem. A*, 2020, **8**, 24353–24367.
29 J. Brus, *Solid State Nucl. Magn. Reson.*, 2000, **16**, 151–160.
30 A. W. Schlueter, R. A. Jacobson and R. E. Rundle, *Inorg. Chem.*, 1966, **5**, 277–280.
31 N. Krüger, S. Belz, F. Schossau, A. A. Haghighirad, P. T. Cong, B. Wolf, S. Gottlieb-Schoenmeyer, F. Ritter and W. Assmus, *Cryst. Growth Des.*, 2010, **10**, 4456–4462.
32 E. L. Hahn, *Phys. Rev.*, 1950, **80**, 580–594.
33 D. J. Kubicki, D. Prochowicz, A. Pinon, G. Stevanato, A. Hofstetter, S. M. Zakeeruddin, M. Grätzel and L. Emsley, *J. Mater. Chem. A*, 2019, **7**, 2326–2333.
34 F. Ji, F. Wang, L. Kobera, S. Abbrent, J. Brus, W. Ning and F. Gao, *Chem. Sci.*, 2021, **12**, 1730–1735.
35 A. R. Haase, M. A. Kerber, D. Kessler, J. Kronenbitter, H. Krüger, O. Lutz, M. Müller and A. Nolle, *Z. Naturforsch., A: Phys., Phys. Chem., Kosmophys.*, 1977, **32**, 952–956.
36 S. Hayashi and K. Hayamizu, *Bull. Chem. Soc. Jpn.*, 1991, **64**, 685–687.
37 A. R. Lim, J. K. Jung and S. Y. Jeong, *J. Phys. Soc. Jpn.*, 2002, **71**, 332–335.
38 A. R. Lim, *Appl. Magn. Reson.*, 2017, **48**, 889–899.
39 K. Jeronimo, V. Koutsos, R. Cheung and E. Mastropaolo, *Sensors*, 2021, **21**, 5873.